


Article

Numerical and Experimental Analysis of the Effect of a Swirler with a High Swirl Number in a Biogas Combustor

Marco Osvaldo Viguera-Zúñiga^{1,2}, Carlos Augusto Ramírez-Ruíz¹, Agustín L. Herrera-May^{1,3} 
and María Elena Tejeda-del-Cueto^{1,2,*}

¹ Faculty of Engineering of the Construction and Habitat, Universidad Veracruzana, Veracruz 94294, Mexico; mviguera@uv.mx (M.O.V.-Z.); zs18024825@estudiantes.uv (C.A.R.-R.); leherrera@uv.mx (A.L.H.-M.)

² Mechanical Engineering Department, Universidad Veracruzana, Veracruz 94294, Mexico

³ Micro and Nanotechnology Research Center, Universidad Veracruzana, Veracruz 94294, Mexico

* Correspondence: etejeda@uv.com

Abstract: Climate change as a worldwide phenomenon is the cause of multinational agreements such as the Kyoto Protocol and the Paris Agreement with the goal of reducing greenhouse gas emissions. Biogas is one of the most promising biofuels for the integration of clean energy sources; however, biogas has the disadvantage of a low calorific value. To overcome this problem, mechanical devices such as swirlers are implemented in combustion chambers (CCs) to increase their combustion efficiencies. A swirler induces rotation in the airstream that keeps a constant re-ignition of the air–fuel mixture in the combustion. We present the numerical modeling using computational fluid dynamics (CFD) and experimental testing of combustion with biogas in a CC, including an optimized swirler in the airstream with a swirl number (S_n) of 2.48. A turbulence model of the renormalization group (RNG) was used to analyze the turbulence. Chemistry was parameterized using the laminar flamelet model. The numerical model allows visualizing the recirculation zone generated at the primary zone, and partially at the intermediate zone of the CC caused by the strong swirl. Temperature distribution profiles show the highest temperatures located at the intermediate and dilution zones, with the last one being a characteristic feature of biogas combustion. A strong swirl in the airstream generates low-velocity zones at the center of the CC. This effect centers flame, avoiding hot spots near the flame tube and flashback at the structural components. Regarding pollutant emissions, the goal of a biogas that generates less pollutants than nonrenewable gases is accomplished. It is observed that the mole fraction of NO in the CC is close to zero, while the mole fraction of CO₂ after combustion is lowered compared to the original mole fraction contained in the biogas (0.25). The mole fraction of CO₂ obtained in experimental tests was 0.0127. Results obtained in the numerical model for temperatures and mole fractions of CO₂ and NO show a behavior similar to that of the experimental model. Experimental results for mole fraction of CO emissions are also presented and have a mean value of 0.0009. This value lies within allowed pollutant emissions for CO according to national environmental regulations.

Keywords: biogas; strong swirl; optimized swirler; combustion chamber; pollutant emissions



Citation: Viguera-Zúñiga, M.O.; Ramírez-Ruíz, C.A.; Herrera-May, A.L.; Tejeda-del-Cueto, M.E. Numerical and Experimental Analysis of the Effect of a Swirler with a High Swirl Number in a Biogas Combustor. *Energies* **2021**, *14*, 2768. <https://doi.org/10.3390/en14102768>

Academic Editor: John James Milledge

Received: 20 April 2021

Accepted: 8 May 2021

Published: 12 May 2021

Publisher's Note: MDPI stays neutral with regard to jurisdictional claims in published maps and institutional affiliations.



Copyright: © 2021 by the authors. Licensee MDPI, Basel, Switzerland. This article is an open access article distributed under the terms and conditions of the Creative Commons Attribution (CC BY) license (<https://creativecommons.org/licenses/by/4.0/>).

1. Introduction

1.1. Biogas

Biogas is a biofuel that offers an important scenario when talking about alternative fuels to generate energy [1–4]. It is used as a power source to produce heat or steam and electric power and as a vehicle fuel [5,6]. Biogas is a product of the decomposition of organic waste in the absence of O₂, and it is widely produced in landfills or anaerobic digesters [7]. Volumetric fraction of CH₄ in biogas has a range of 50–75% [8], with CO₂ being the remaining percentage. The use of biogas is becoming popular in gas turbine combustors because it reduces dependence on fossil fuels [9–13], and it is commonly used

in hybrid systems combining solar energy and biogas for generating electric power in a 60 kW nominal power plant [11]. Biogas can be used pure or mixed with other fuels to obtain a better performance [3,14–17].

Biogas combustion offers the advantage of reducing the presence of CH₄ [18] and CO₂ [10], which are greenhouse gases, in the atmosphere. The most important reaction for CO₂ formation in this type of flame is $\text{CO} + \text{OH} \rightleftharpoons \text{CO}_2 + \text{H}$. Additionally, CO₂ competes with O₂ to gain H radicals through the reversible chain reaction $\text{H} + \text{O}_2 \rightleftharpoons \text{O} + \text{OH}$ [14], reducing the presence of radicals. CO₂ in fuel presents a negative effect in dilute flames elongating the reaction zone in the axial direction when the dilution rate increases. Commonly, the reaction zone is dragged by the flow, and combustion areas are separated by a noncombustion zone [15]. CO₂ in biogas reduces flame temperature [19,20]; this is mainly observed during fuel injection where mole fraction of CO₂ is the highest, which adversely affects flame temperature. From this point, the mole fraction of CO₂ decreases as the axial distance is increased inside the CC; therefore, flame temperature increases.

The presence of CO₂ in the biogas also contributes to NO_x reduction [21,22]. This effect is enhanced if there is uniform mixing of the air and fuel streams.

1.2. Types of Flames

There are two main types of flames: premixed flames and non-premixed flames. In premixed flames, air mixes with fuel inside the burner, and the downstream mix is ignited. According to Peters [23], premixed combustion is characterized by the laminar burning velocity. This is the velocity at which the flame front propagates in the mixture of air and fuel reactants. Premixed flames are used when a high-intensity flame is required within a small volume.

Non-premixed flames are also known as diffusion flames. A characteristic of these flames is that air is not mixed with fuel inside the burner. Bilger [24] states that mixing is done through diffusion. Non-premixed combustion is basically controlled by mixing. Veynante [25] addresses that flame is mainly controlled by the uniform mixing given by fresh gases. Large combustion devices such as combustion chambers or combustors work under non-premixed conditions. This is mainly because the premixing of large volumes represents serious safety problems [23].

1.3. Effect of Swirling Flows in Flames

In non-premixed flames, uniform mixing can be achieved by injecting fuel into the airstream with proper swirl intensity. Swirl number (S_n) is related to creating recirculation under conditions of high-intensity flow with $S_n > 0.6$. Swirl number stabilizes the flame by inducing recirculation of hot products that generate constant re-ignition in the air and fuel streams entering a combustor. Swirling flows with a sufficient amount of turbulence are required to induce a reverse flow and define a recirculation zone [9,15,21,22,26–29]. An increment in swirl number leads to higher recirculation [30]. Beer and Syred [31] indicated that flows with high-intensity turbulence have a range of swirl numbers between 0.6 and 2.5. Several studies have analyzed the variation of swirl to improve combustion in flames [9,10,15,16,29,32–35].

Currently, computational tools allow researchers to generate close-to-reality models in order to test their theories without having to build a prototype for testing [22,36]. This represents an advantage in making it possible to predict a phenomenon behavior and make corrections to designs before they are built. Several investigations have been carried out not only in swirling induced combustion chambers (CCs) [4,29,33,37–39] but also in biogas-powered CCs [3,7,16], as well as on their corresponding behavior regarding pollutant emissions [37,40–42], obtaining similar results to the experimental models. In order to better match experimental results with the numerical model, it is necessary to select the correct turbulence model. There are three mathematical models to perform numerical analysis of turbulence in CFD: direct numerical simulation (DNS) [43], large eddy simulation (LES), and Reynolds-averaged Navier–Stokes simulation (RANS) [44,45].

DNS is limited to low and moderate Reynolds numbers as well as simple geometries. This feature is caused by the necessity of having a highly refined mesh in order to have acceptable results [46]. Ying Wen [47] states that some restrictions prevent using DNS in gas turbine combustors. On the other hand, Bulat [48] describes the LES turbulence model as a powerful and promising modeling technique applied particularly to unsteady flows with high induced swirl. Giacomazzi [49] concludes that LES generates better results than other turbulence models for nonreactant flows. Its main disadvantage is the dependency on mesh resolution and computational resources needed. RANS model is a viable alternative because it solves practical problems with low computational cost [50]. Furthermore, it has three two-equation submodels, the standard $k-\epsilon$ model, the $k-\epsilon$ RNG model, and the realizable $k-\epsilon$ model. Additionally, RANS has a seven-equation model known as the Reynolds stress model (RSM). RANS models used for modeling swirl in turbulent flames are the RSM and the $k-\epsilon$ RNG. RSM model has been used to simulate combustion in non-premixed flames with good results regarding matching experimental data [30,51]. On the other hand, $k-\epsilon$ RNG model has been used by researchers such as Widmann et al. [52]; they modeled the air flow passing through a vane cascade swirl generator in a combustion reactor. Reported results showed a velocity profile consistent with experimental measurements. Darwaman [53] developed the numerical model for air flow entering the combustion chamber of a micro gas turbine using two turbulence models; one of them was $k-\epsilon$ RNG. Numerical results matched velocity and pressure measurements, mainly at the swirling flow region. A year later, Khaldi [54] studied the numerical model of the combustion of a 300 MWe tangentially fired pulverized coal furnace; this study used several turbulence models and concluded that the $k-\epsilon$ RNG model is the most suitable to predict velocity and temperature profiles. Zavaleta [29] designed an optimized swirler with a high swirl number using genetic algorithms; additionally, it was fabricated, tested, and compared to the CFD numerical model of a combustion chamber with non-premixed flame. His results indicated that the $k-\epsilon$ RNG model is suitable to predict temperature profiles.

In this work, we employed numerical modeling and experimental testing to study the combustion of biogas in a combustion chamber with an optimized swirler ($Sn = 2.48$). The swirler was optimized for this combustion chamber as its final geometry was determined by considering the following parameters: minimum pressure drop, air mass flow, maximum swirl number to stabilize flame, and physical dimensions of the combustion chamber. Flame behavior was analyzed using computational fluid dynamics (CFD) with boundary conditions similar to real operating environments. As expected, the presence of CO_2 in biogas dragged the reaction zone in the axial direction, thus developing the highest temperature region where the mole fraction of CO_2 was lower when compared to the initial mole fraction from biogas; however, a flame without noncombustion zones was obtained. Subsequently, the numerical model was validated using experimental test data containing among several variables the mole fractions of CO_2 and NO .

2. Experimental Setup

The non-premixed flame combustion chamber used in this work has a casing made of SAE 1045 steel; flame tube inside the casing is made out of 304 stainless steel; diffuser and nozzle are made of SAE 1045 steel; fuel injector is made of 304 stainless steel and has 6 radially distributed holes. The combustion chamber is shown in Figure 1.

The CC has three zones, and each zone has a specific purpose. The primary zone anchors and stabilizes the flame. This zone uses an optimized swirler with an Sn of 2.48 [29], and it has 8 vanes 1 mm thick equally distributed at an angle of 18° . Vane depth is 3.9 cm, and its hub diameter (D_{hub}) is 5.76 cm as shown in Figure 2.

The function of the intermediate zone is to decrease gas temperature, allowing combustion of CO and CH . The intermediate zone has 5 holes with a diameter of 0.476 cm. These holes are drilled around the flame tube and are located at $L = 18$ cm measured from the inlet of the CC.

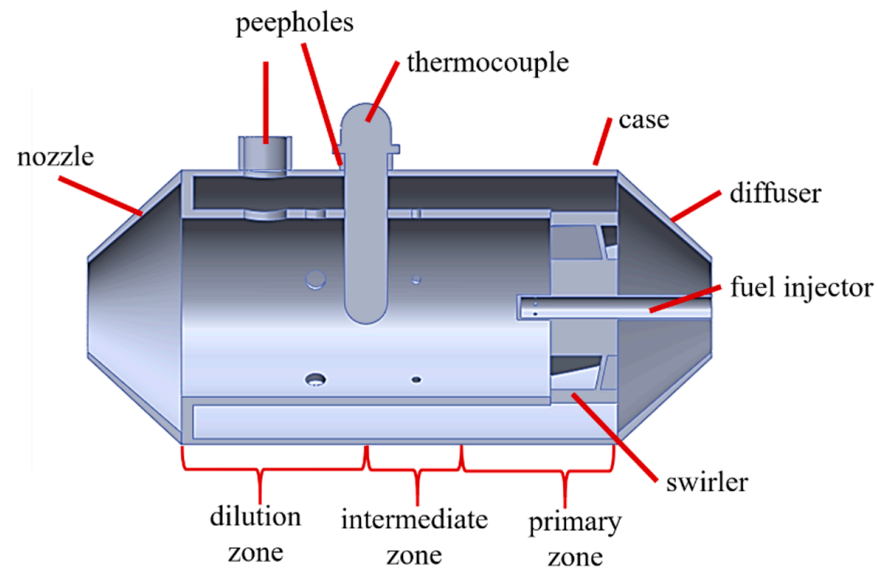


Figure 1. Non-premixed flame combustion chamber with swirler.

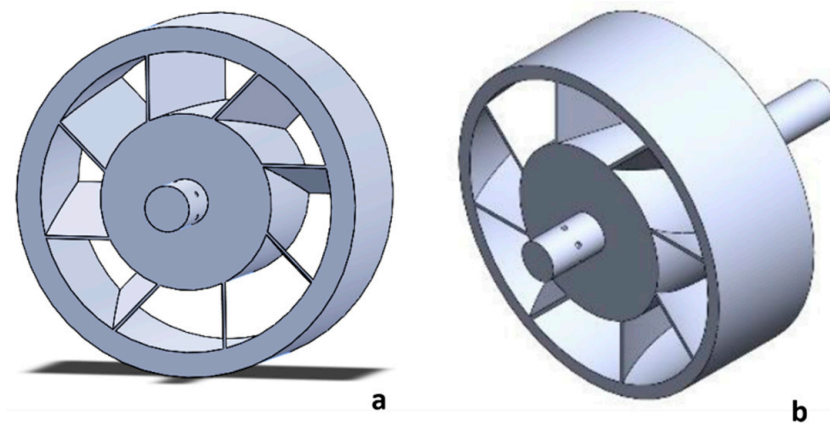


Figure 2. Optimized swirler with fuel injector: (a) front view; (b) isometric view.

The dilution zone cools down the flame to obtain an appropriate temperature at the outlet of the CC. This zone is located at $L = 24$ cm from the inlet of the CC.

3. Numerical Model

3.1. Fuel Composition

Chemical fuel composition of biogas from the supply line has following mole fractions: methane = 0.75 and CO_2 = 0.25 [8,42,55].

3.2. Mesh Characteristics

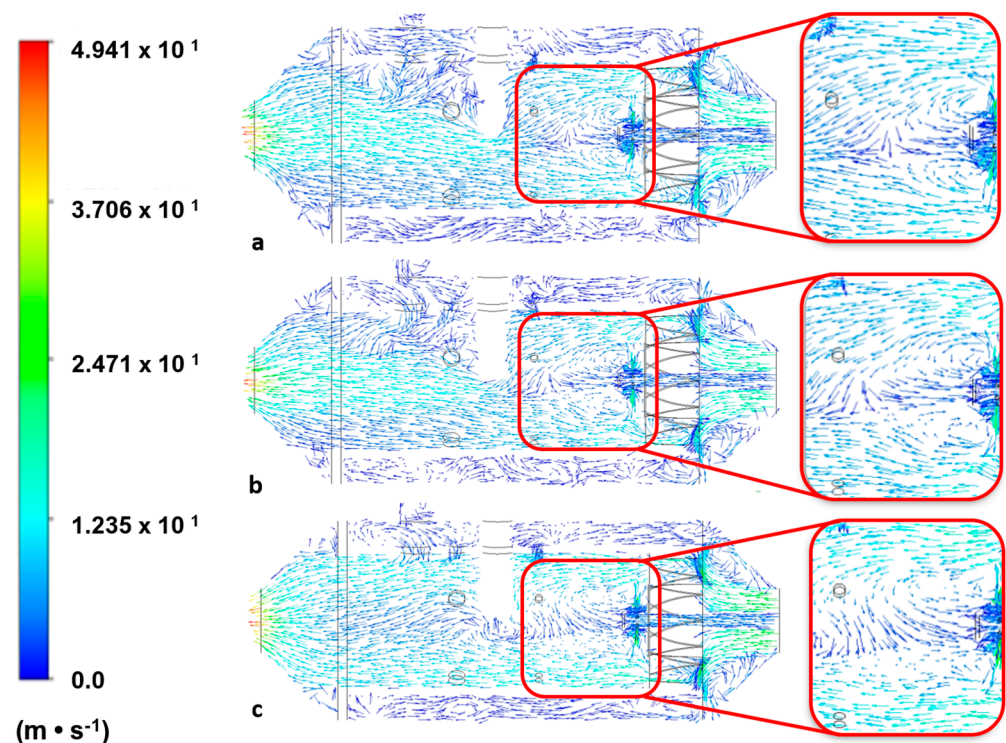
A CFD model of the combustion chamber was developed to study its performance using the finite volume method in Fluent ANSYS [56].

Mesh sensitivity analysis was performed on three meshes to determine the effects of mesh size on CFD results to guarantee that the aforementioned results are mesh-independent. Differences among the meshes were in mainly mesh density and the corresponding numbers of elements and nodes. Mesh parameters of the three meshes are presented in Table 1.

Table 1. Features of three meshes for mesh sensitivity analysis.

Parameter	Mesh 1	Mesh 2	Mesh 3
Number of elements	6,740,626	5,229,172	4,181,507
Number of nodes	1,208,676	943,529	755,893
Face size	2	2	1
Edge Sizing number	40	40	30
Growth rate	1.2	1.2	1.2
Maximum orthogonality	0.771	0.758	0.758
Minimum obliquity	0.229	0.242	0.242

Figure 3 shows a comparison of velocity vectors from meshes under analysis. It can be observed in Figure 3a,b that velocity vectors depict a similar behavior regarding a central recirculation zone with low magnitude velocities at the primary zone mainly observed from $r = 0$ up to D_{hub} ; it can also be observed that velocity increases from D_{hub} up to the internal wall of the flame tube. The aforementioned central recirculation region and its corresponding swirl are located only at the primary zone of the combustion chamber; as the flow passes downstream to intermediate and dilution zones, velocity increases and swirl vanishes. On the other hand, in Figure 3c, the central recirculation region at the primary zone is narrower and longer than in meshes 1 and 2. It is observed that low velocity vectors remain at the center line of the combustion chamber through the intermediate and dilution zones.

**Figure 3.** Comparison of velocity vector profiles at central longitudinal plane: (a) mesh 1; (b) mesh 2; (c) mesh 3.

Even though velocity vectors in meshes 1 and 2 had similar behavior, mesh 1 was selected to obtain results to better match experimental measurements of temperatures and emission gases, as will be shown further in this article. Mesh 1 has high-quality obliquity (minimum 0.229) and orthogonality (maximum 0.771) of the elements to increase solution accuracy [43] and improve processing time [57].

Mesh 1 is shown in Figure 4, and boundary conditions are shown in Table 2. Residuals for continuity, momentum, turbulent kinetic energy, mixture fraction, and variance of mixture fraction were set to 1×10^{-4} , while for energy it was 1×10^{-7} .

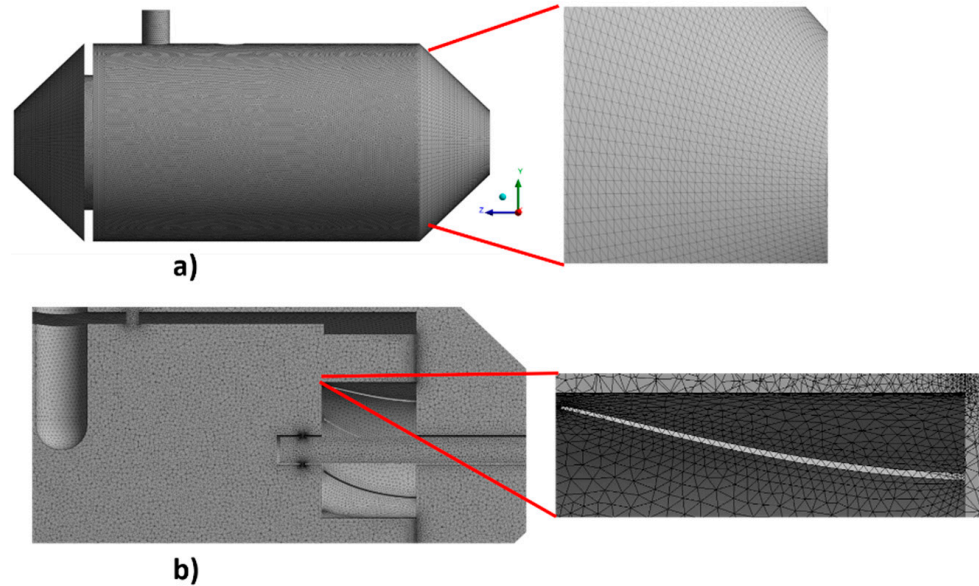


Figure 4. Mesh of fluid volume in the combustion chamber: (a) face size application; (b) swirler vane after using edge sizing number tool.

Table 2. Boundary conditions for numerical analysis.

Parameter	Value
Air inlet pressure (Pa)	2100
Mass air flow (kg/s)	0.04398
Air temperature (K)	305.15
Fuel temperature (K)	301.15
Fuel inlet pressure (Pa)	2100
Mass fuel flow (kg/s)	0.0004996
Combustion chamber outlet pressure (Pa)	375
Wall temperature (K)	300

3.3. Turbulence Model

The k - ε RNG turbulence model is a variation of the k - ε standard derived by Yakhot and Orszag [58]. The k - ε RNG model is mainly used in swirling flows, providing results with an acceptable approximation to experimental data [29,46,59]. To derive the RNG model, a mathematical technique was applied to the Navier–Stokes equations called the “renormalization group” method. It assumes that flow is fully turbulent with negligible molecular viscosity effects [60]. Model equations are as follows:

$$\frac{\partial(\rho k)}{\partial t} + \frac{\partial(\rho u_j k)}{\partial x_j} = \frac{\partial}{\partial x_j} \left[\left(\mu + \frac{\mu_t}{\sigma_k} \right) \frac{\partial k}{\partial x_j} \right] + \mu_t \left(\frac{\partial u_i}{\partial x_j} + \frac{\partial u_j}{\partial x_i} \right) \frac{\partial u_i}{\partial x_j} - \rho \varepsilon \quad (1)$$

$$\frac{\partial(\rho \varepsilon)}{\partial t} + \frac{\partial(\rho u_i \varepsilon)}{\partial x_i} = \frac{\partial}{\partial x_j} \left[\left(\left(\mu + \frac{\mu_t}{\sigma_\varepsilon} \right) \frac{\partial \varepsilon}{\partial x_j} \right) \right] + C_\varepsilon^* \mu_t \frac{\varepsilon}{k} \left(\frac{\partial u_i}{\partial x_j} + \frac{\partial u_j}{\partial x_i} \right) \frac{\partial u_i}{\partial x_j} - C_{\varepsilon 2} \rho \frac{\varepsilon^2}{k} \quad (2)$$

with

$$\mu_t = \rho C_\mu \frac{k^2}{\varepsilon} \quad (3)$$

$$C_{\varepsilon 1RNG} = 1.42 - \frac{\eta \left(1 - \frac{\eta}{\eta_0}\right)}{(1 - \beta\eta^3)} \quad (4)$$

$$\eta = \sqrt{\mu_t \left(\frac{\partial u_i}{\partial x_j} + \frac{\partial u_j}{\partial x_i} \right) \left(\frac{\partial u_i}{\partial x_j} / \rho C_{\mu} \varepsilon \right)} \quad (5)$$

where the term μ_t represents turbulent viscosity and constant values are as follows: $C_{\mu} = 0.085$, $C_{\varepsilon 2} = 1.68$, $\sigma_{\varepsilon} = 1.3$, $\sigma_k = 1.0$, $\beta = 0.015$, and $\eta_0 = 4.38$.

3.4. Laminar Flamelet Model

Combustion is a chemically difficult process to analyze due to a large number of intermediate reactions taking place. Some numerical models of turbulent combustion are based on modeling combustion in a one-step reaction using only the fuel and the oxidant, neglecting molecular transport [36]. The laminar flamelet model proposed by Peters [61] provides detailed chemistry to focus on flame-relevant conditions [62]. It is used to obtain more accurate solutions for species equations involved in the chemical kinetics mechanism of combustion. In non-premixed flames, this model solves the chemical kinetics of combustion in terms of two variables, the mixture fraction (Z) and the scalar dissipation χ . Mass fraction Y_i and the temperature T [21,29,63] are also considered in the flamelet equations.

$$\rho \frac{\partial Y_i}{\partial t} = \rho \frac{\chi}{2} \frac{\partial^2 Y_i}{\partial Z^2} + w_i - \rho \left(\frac{D\chi}{2} \right)^{\frac{1}{2}} k \frac{\partial Y_i}{\partial Z} \quad (6)$$

$$\rho \frac{\partial T}{\partial t} = \rho \frac{\chi}{2} \frac{\partial^2 T}{\partial Z^2} + w_T - \rho \left(\frac{D\chi}{2} \right)^{\frac{1}{2}} k \frac{\partial T}{\partial Z} \quad (7)$$

where w_T and w_i represent the chemical components for temperature and species, respectively. k is the curved isoline of the mixture fraction, and t is the time. The mixture fraction is a conserved scalar representing the element mass fractions (equation 9). The scalar dissipation rate (χ) is defined in Equation (8) [64], which represents flame stretching [63].

$$\chi = 2D|\nabla z|^2 \quad (8)$$

$$\rho \frac{\partial Z}{\partial t} + \rho v_k \frac{\partial Z}{\partial \chi} = \frac{\partial}{\partial \chi} \left[\rho D \frac{\partial Z}{\partial \chi} \right] \quad (9)$$

where D is the diffusion coefficient and v_k is the velocity.

In this study, the chemical kinetics mechanism for biogas from the University of San Diego [65] was used. It has 58 species, including CO and CO₂, and 270 reactions. The thermal NO_x formation mechanism was used to analyze NO.

4. Numerical Modeling Results

Figure 5 shows six planes parallel to the xy plane of the combustion chamber, which were used to obtain the results of numerical modeling. Table 3 describes the z location from the origin for each plane.

Table 3. The z location from the origin for planes.

Plane	Distance from Origin (cm)	Plane	Distance from Origin (cm)
a	10.4	d	23.6
b	14	e	26.6
c	17.6	f	30

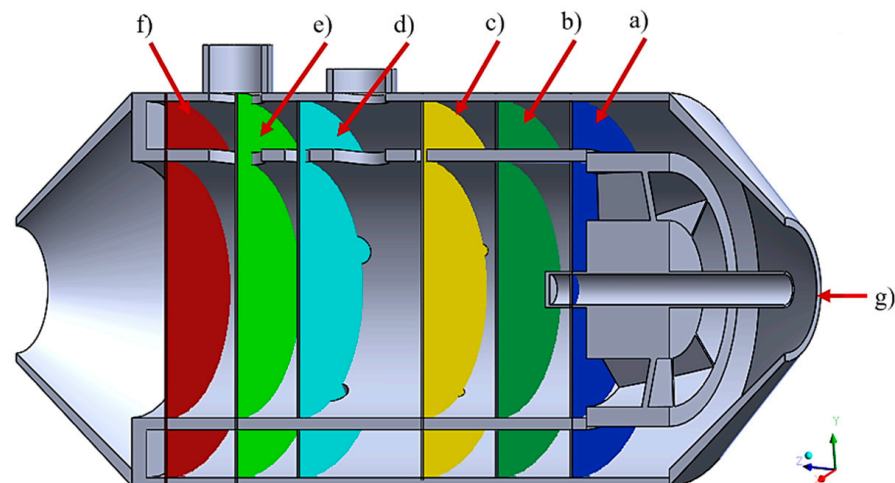


Figure 5. View of xy planes and origin of the combustion chamber: (a) plane 1; (b) plane 2; (c) plane 3; (d) plane 4; (e) plane 5; (f) plane 6; (g) origin.

4.1. Velocity Profile

Air flow velocity inside the CC is highly important for the combustion process. If air flow entering the combustion chamber has a low velocity, this could cause flame flashback [66,67].

Figure 6a shows a side view of streamlines during combustion inside the CC, while Figure 6b depicts a top view. Both figures show swirling in the streamlines mainly in the primary zone with a swirling decreasing effect as it approaches the dilution zone.

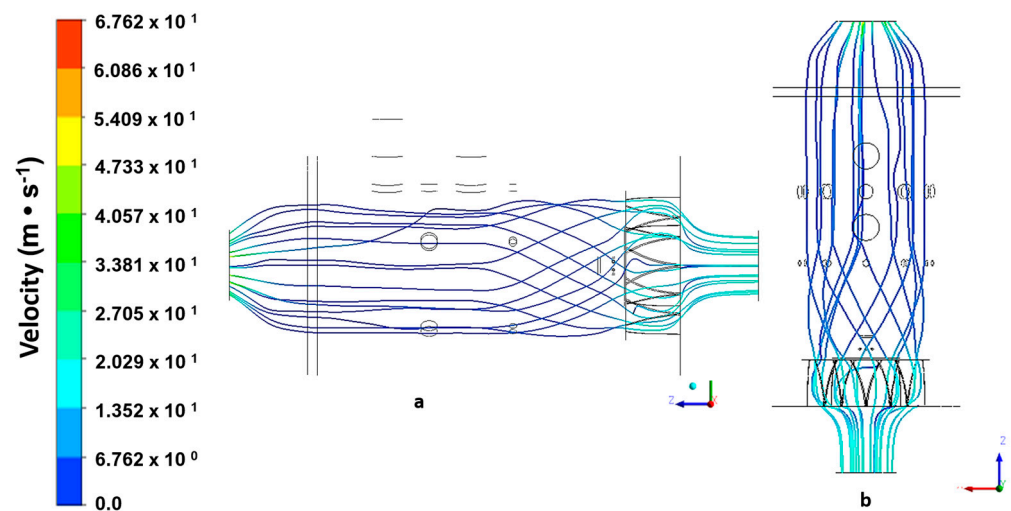


Figure 6. Flow streamlines in the combustion chamber: (a) side view yz plane; (b) top view xz plane.

Figure 7 shows velocity profiles at the six transverse xy planes in the combustion chamber during the combustion process. In Figure 7a, a uniform velocity distribution is observed across the flame tube except at the fuel injection, where the highest velocity (20.29 m/s) is obtained. Figure 7b depicts a velocity profile increasing radially from the center outwards with a predominant speed of 6.7 m/s. This low velocity is caused by the recirculation effect observed in Figure 6. Figure 7c exhibits that region between D_{hub} and radius = 0 has a zone of lower recirculation compared to the rest of the space delimited by the inner radius of the flame tube. At radius = 0, there is a zone of velocities of similar magnitude to those found at the swirler vanes, which represents fuel injection velocity. Figure 7d–f shows similar velocity profiles with variations at the air inlets of the flame tube.

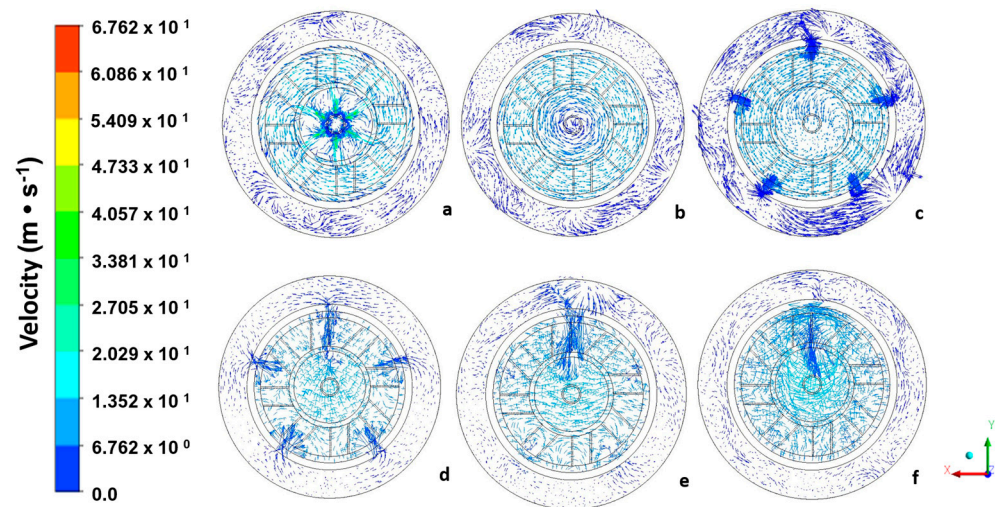


Figure 7. Combustion velocity profiles at transverse planes: (a) plane 1; (b) plane 2; (c) plane 3; (d) plane 4; (e) plane 5; (f) plane 6.

4.2. Combustion Profiles

Figure 8 shows temperature profiles at transverse planes of the combustion chamber. It is observed that flame is centered in every plane. Figure 8a depicts the highest temperature region located between D_{hub} and $r = 0$; this temperature is reached near each fuel injection orifice caused by the highest mixture fraction (Z). In Figure 8b, the flame extends from $r = 0$ up to the middle section of the vanes, covering a large part of the flame tube; however, the magnitude of temperatures is lower than that in Figure 8a. Figure 8c exhibits flame covering the same section as in Figure 8b with a more uniform profile and higher average temperature. Figure 8d indicates an increase in flame temperature with the highest temperature located close to the center; as the radius increases until reaching D_{hub} , the temperature has a progressive decrease, and at that point decreases drastically. It can also be observed that the flame is drifted down on the y -axis. In Figure 8e, the flame is more drifted on the y -axis, keeping a higher temperature at the center. Figure 8f depicts a similar behavior to that in the previous plane with a smaller high-temperature region given by fewer points in the cross-section with a high mixing fraction.

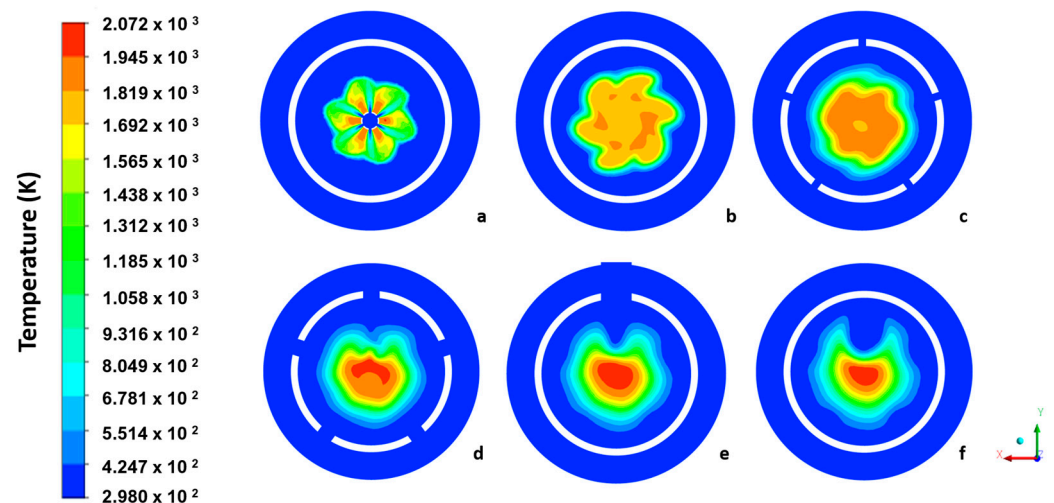


Figure 8. Temperature profiles at transverse plane of the combustion chamber: (a) plane 1; (b) plane 2; (c) plane 3; (d) plane 4; (e) plane 5; (f) plane 6.

As observed in Figure 9, the flame is centered in the combustion chamber caused by the swirler. The region with higher temperatures is located at the intermediate and dilution

zones; this is a characteristic feature of biogas flames. A relevant observation in Figure 9 is that there are no transverse planes with the absence of combustion; i.e., the mixture fraction is significant for each plane.

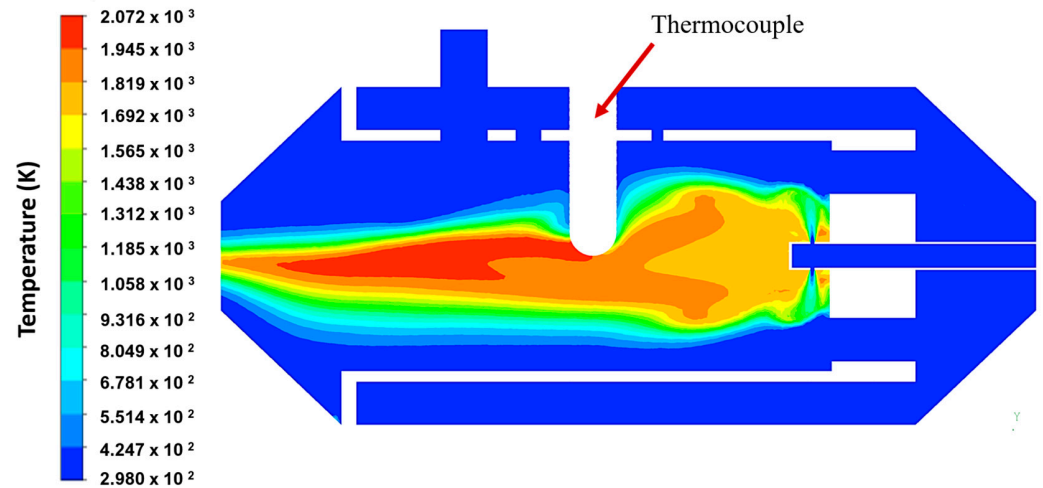


Figure 9. Temperature profile at longitudinal plane at the center of the combustion chamber.

In Figure 10, mole fraction profiles of CO are shown for cross-sectional planes. Figure 10a shows a flower-shaped mole fraction profile of CO, which is mainly concentrated at the region between D_{hub} and $r = 0$ caused by swirl in velocity vectors; the highest local mole fraction is 3.48×10^{-2} . In Figure 10b, the mole fraction increases to 7.83×10^{-2} , and a deformed flower-shaped profile is preserved. In this plane, the highest mole fraction is located at $r = 0$. Figure 10c–f shows the mole fraction of CO decreasing progressively, which indicates that there is a high conversion of reactants because there is a match between temperature and CO generation. This effect occurs when there is enough energy and retention time resulting in a high conversion of CO to CO_2 .

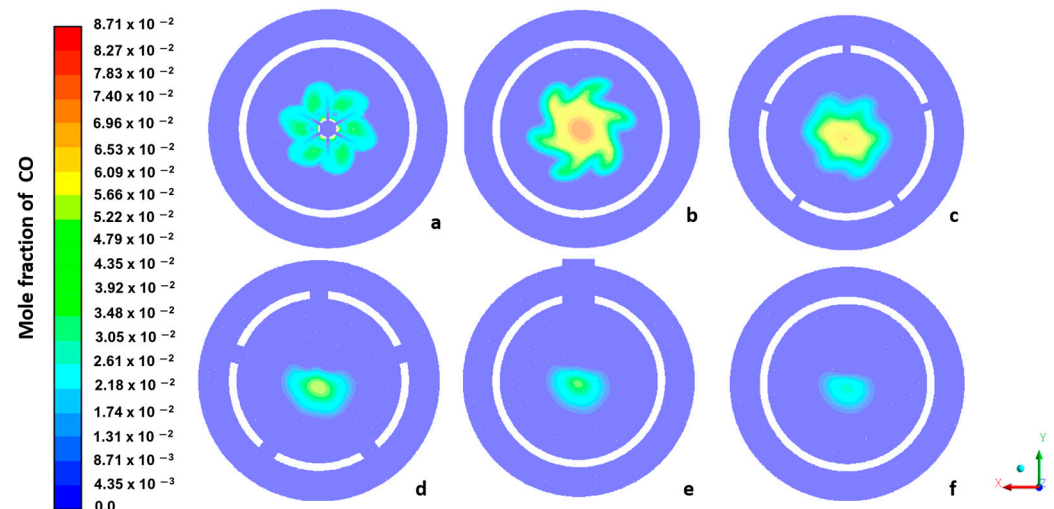


Figure 10. Mole fraction of CO for cross-sectional planes: (a) plane 1; (b) plane 2; (c) plane 3; (d) plane 4; (e) plane 5; (f) plane 6.

Figure 11 depicts mole fraction variation of CO at the outlet of the combustion chamber on the y -axis, i.e., up and down. It is observed that the point of CO formation is below the center of the chamber outlet ($y = 0$); the average value of the mole fraction at the outlet is 1.45347×10^{-4} .

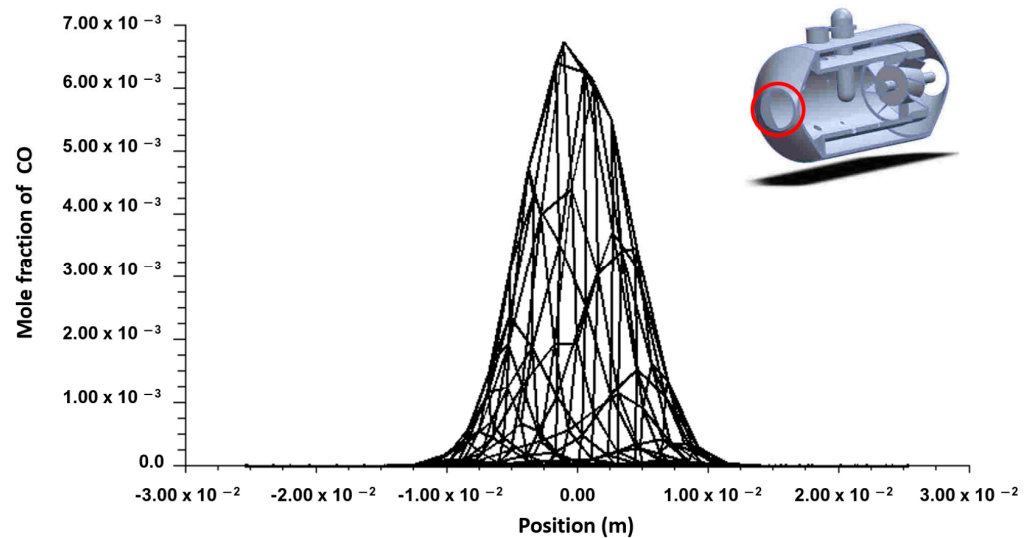


Figure 11. Mole fraction variation of CO at the outlet of the combustion chamber on the y -axis.

Analysis of CO_2 is an important part of this study as it has two roles as reactant and product, as shown in Figure 12. Figure 12a exhibits the highest global mole fraction of CO_2 as it is where fuel is injected with a value of 0.25 corresponding to the biogas mole fraction of CO_2 ; rotation of CO_2 is observed due to swirling of airstream resulting in a flower-like profile with its highest value at the center and a progressive decrease until reaching an approximate mole fraction of 0.0625 at D_{hub} . In Figure 12b, the flower shape remains and is enlarged, covering a larger cross-area of the flame tube, and exhibits a more uniform profile compared to plane 1. Figure 12c shows a quasi-circular shape with similar global minimum and maximum values as in plane 2. In Figure 12d, a decrease is observed in the cross-area, where CO_2 is observed having a similar behavior to that seen in Figure 8d. The mole fraction at the center of the combustion chamber is 0.0625. It is observed that as CO_2 decreases, flame temperature increases [19,20]. In Figure 12e–f, mole fraction of CO_2 decreases in the upper part, maintaining an average mole fraction of 0.0625; this behavior is consistent with the increment in temperature at the hotter spots as in Figure 8e–f.

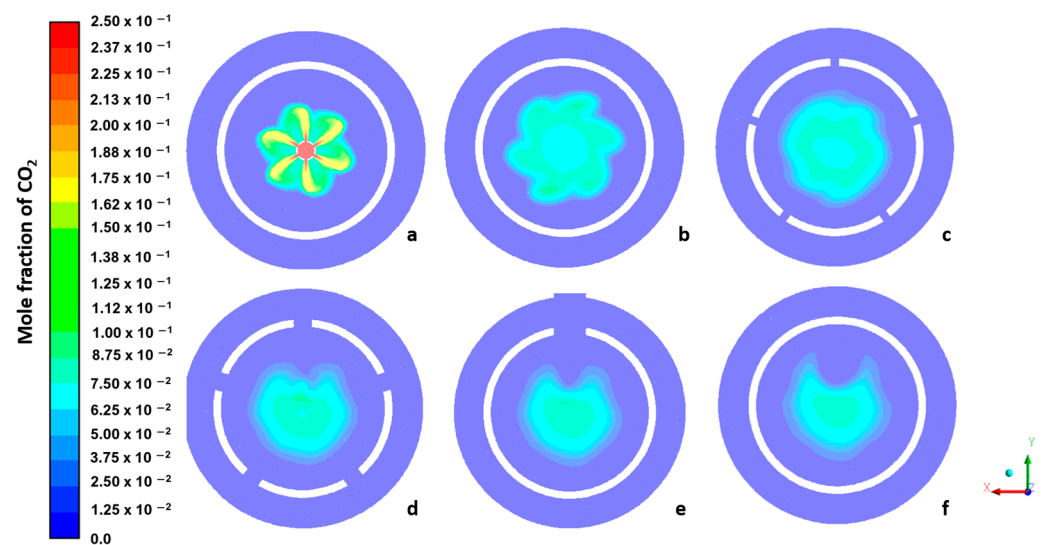


Figure 12. Mole fraction profiles of CO_2 for cross-sectional planes: (a) plane 1; (b) plane 2; (c) plane 3; (d) plane 4; (e) plane 5; (f) plane 6.

Figure 13 indicates mole fraction variation of CO_2 at the outlet of the combustion chamber on the y -axis. The average mole fraction value is 0.01346.

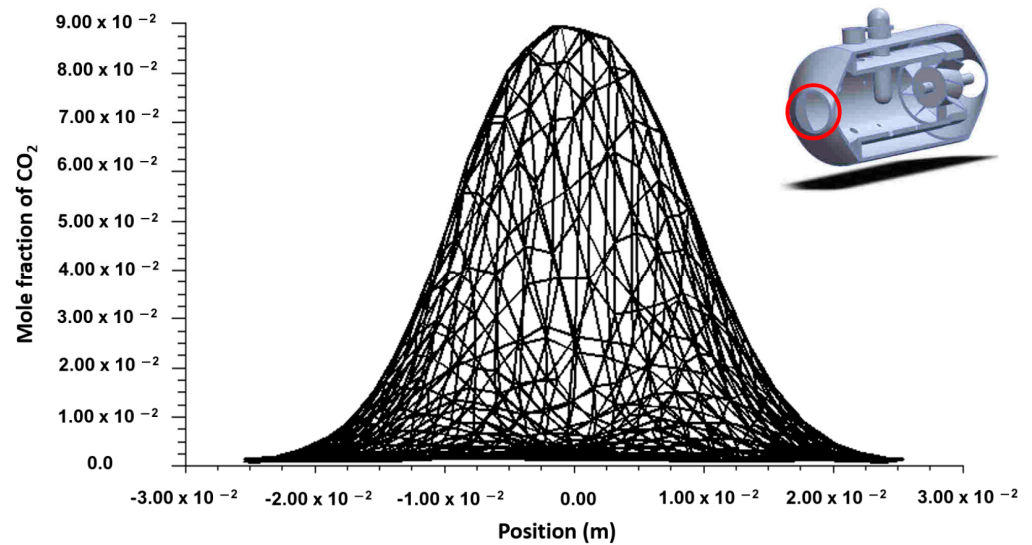


Figure 13. Mole fraction variation of CO₂ at the outlet of the combustion chamber on the *y*-axis.

Figure 14 exhibits the mole fraction of NO at the transverse planes. From Figure 14a, we observed that NO formation begins at the region near fuel injection holes. This point coincides with the region of higher temperature magnitude in Figure 8a. On the other hand, in Figure 14b, NO is found near D_{hub} . In Figure 14c, the distribution profile of NO depicts a lower mole fraction at the center of the combustion chamber compared to the zone close to D_{hub} (mole fraction 5.05×10^{-6}). Figure 14d,e shows an increment in mole fraction of CO (1.77×10^{-5}). In Figure 14f, it can be seen that the mole fraction of NO increased up to 2.27×10^{-5} . Despite these slight increases, NO formation inside the combustion chamber is almost zero.

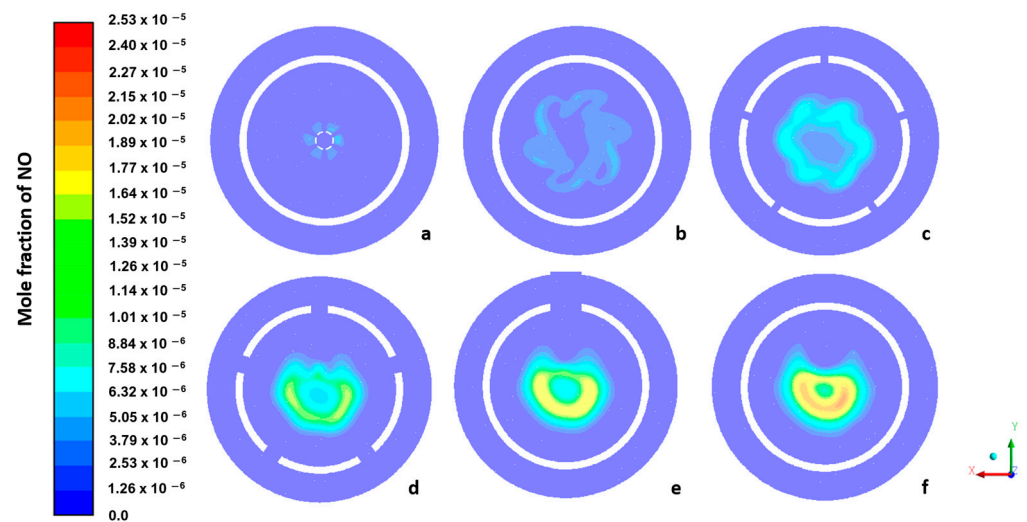


Figure 14. Mole fraction profiles of NO for transverse planes: (a) plane 1; (b) plane 2; (c) plane 3; (d) plane 4; (e) plane 5; (f) plane 6.

Figure 15 reveals that the presence of NO is slightly predominant on the negative *y*-axis. The average mole fraction of NO at the combustion chamber outlet is 2.300062×10^{-6} .

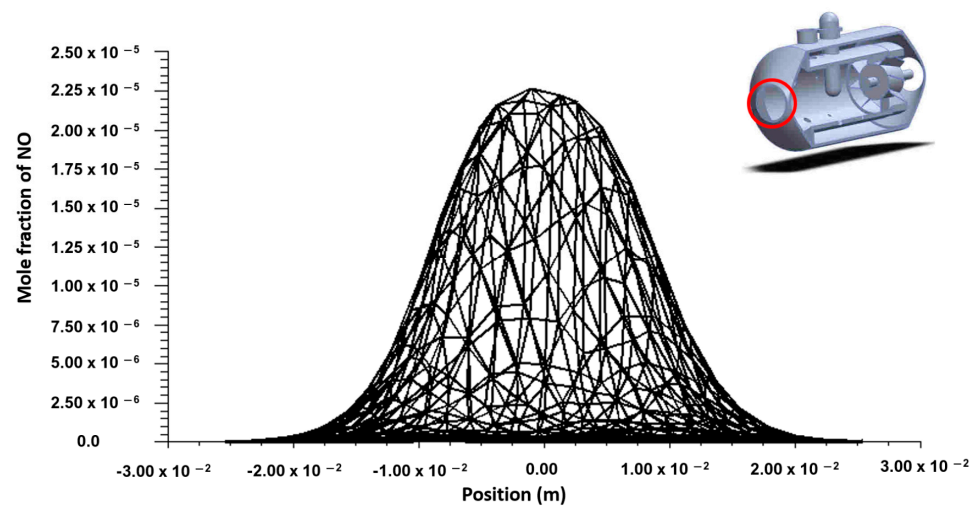


Figure 15. Mole fraction variation of NO at the outlet of the combustion chamber on the y -axis.

5. Experimental Testing

Combustion tests were done at the facilities of the Engineering Department of Universidad Veracruzana. The test rig consisted of several devices to provide fuel and air as well as instruments to measure variables of reactants and combustion as follows: Air supply was provided by a blower, and its flow was measured with a pitot tube and an industrial manometer. Biogas was supplied from an industrial tank with a CONCOA gas pressure regulator in line with a needle valve for a precise regulation; fuel flow was measured with an Omega industrial flow meter with a precision of $\pm 1\%$. Monitoring of exhaust gases was done with an ENERAC model 700AV portable gas analyzer with an NDIR bench-type sensor, which allows direct measurement of CO, CO₂, NO, and CH. Average air temperature and relative humidity were monitored with an Extech model 45160 anemometer. The flame temperature was measured using an R-type bimetallic thermocouple (platinum–rhodium 13%) provided with an insulating rod and a ceramic cover that allows measurements in a range from 0 to 1450 °C with a nominal error of ± 1.5 °C. Figure 16 shows the test rig used during experimental testing. The non-premixed flame combustion chamber is the core of the test rig and has the following features: SAE 1045 steel casing, flame tube made of 304 stainless steel, diffuser and nozzle made of SAE 1045 steel, and fuel injector with 1/2-inch diameter made of 304 stainless steel. This injector protrudes 1 cm downstream from the swirler hub to ensure a uniform distribution of the fuel inside the combustion chamber.

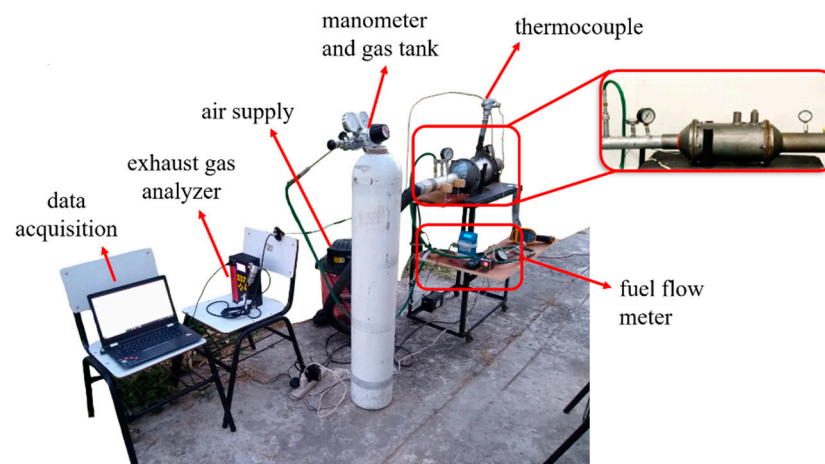


Figure 16. Test rig.

Flame temperature measurements were taken from two peepholes placed on top of the combustion chamber. Four different positions on the y -axis were established at each peephole, taking as reference the central axis of the combustion chamber as shown in Figure 17.

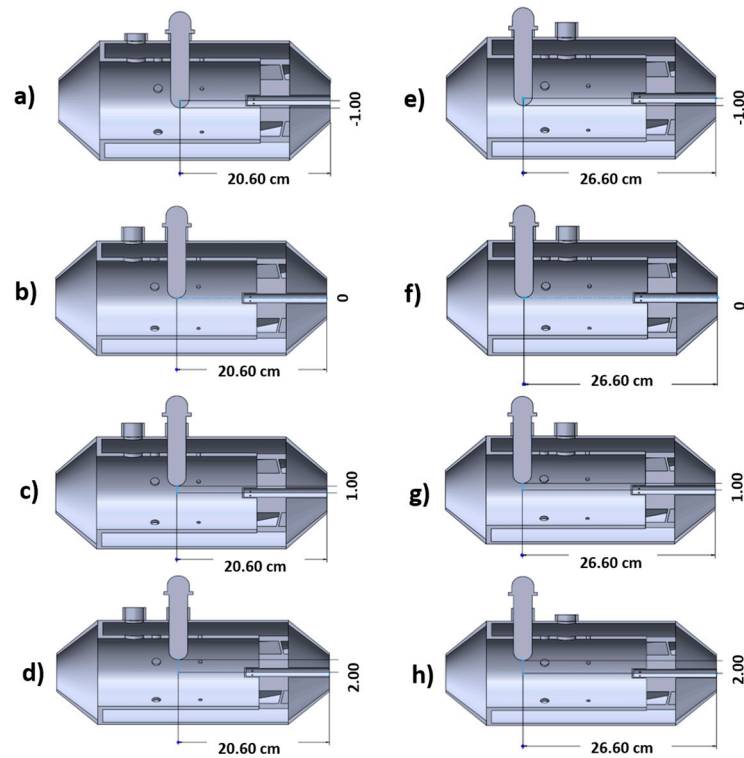


Figure 17. Thermocouple positioned at peepholes. On the left side are shown positions of peephole 1: (a) position 1; (b) position 2; (c) position 3; (d) position 4. On the right side are shown positions of peephole 2: (e) position 5; (f) position 6; (g) position 7; (h) position 8.

Figure 18 shows averaged temperature measurements for eight positions corresponding to both peepholes. For peephole 1, the highest temperature was measured at position 1 with an average temperature of 487 K, and the lowest temperature was located at position 4 with an average value of 345 K. For peephole 2, same trend was found, with the highest average temperature of 443 K taken at position 5 and lowest temperature of 365 K evaluated at position 8.

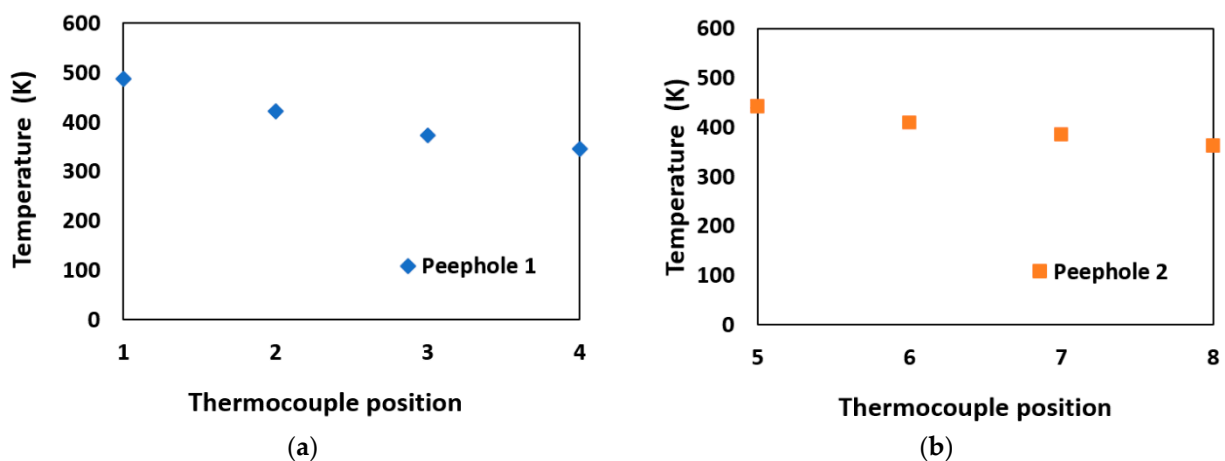


Figure 18. Average temperature measurements at each thermocouple position: (a) peephole 1; (b) peephole 2.

Validation of Numerical Modeling

Figure 19 depicts temperature comparison between numerical modeling and experimental results at peephole 1. Results obtained using CFD have similar behavior to experimental results. The highest temperature differential between numerical and experimental models was obtained at position 1; as the thermocouple moves away from $r = 0$, temperature differential decreases until it is practically zero at position 4. The numerical value of temperature at position 4 lies within 5% uncertainty; meanwhile, the numerical values of temperature at positions 2 and 3 lie within 10% uncertainty [68].

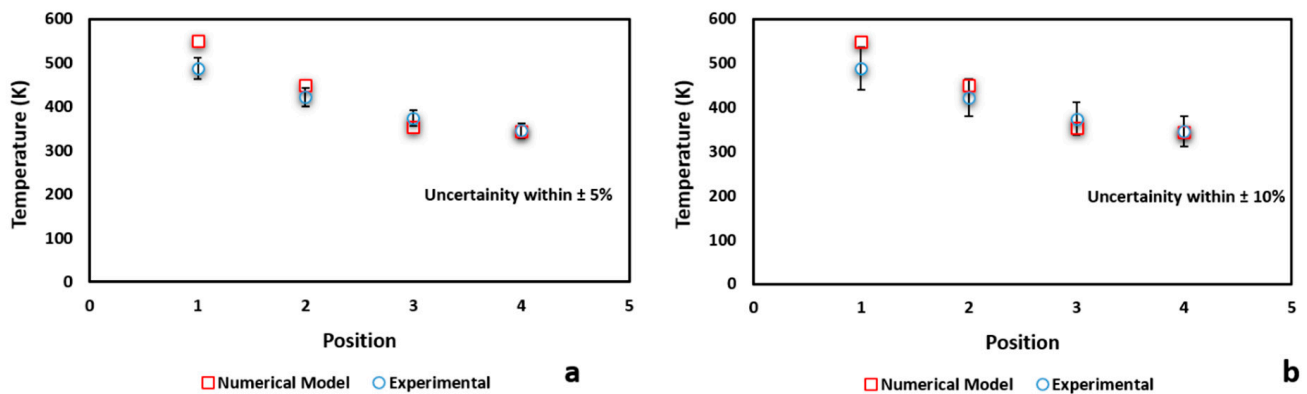


Figure 19. Temperatures measured at peephole 1 obtained using CFD model and experimental tests: (a) 5% uncertainty; (b) 10% uncertainty.

Figure 20 depicts data from numerical modeling and experimental results measured at peephole 2. The numerical model gives a trend similar to that observed with experimental results. The highest temperature differential is measured at position 5, and as the thermocouple moves away from the chamber center, the temperature differential decreases until it is nearly zero at position 8. The numerical value of temperature at position 8 lies within 5% uncertainty; meanwhile, the numerical values of temperature at positions 6 and 7 lie within 10% uncertainty [68].

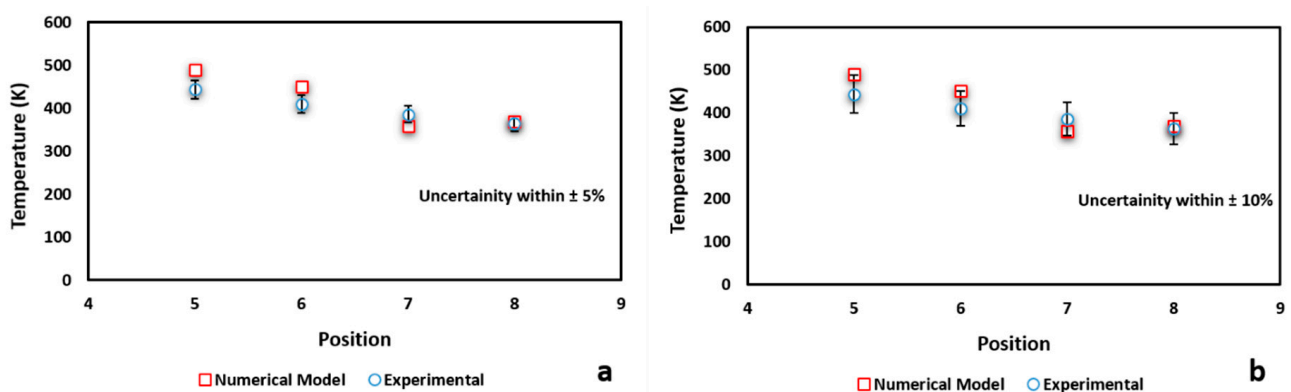


Figure 20. Temperatures measured at peephole 2 obtained using CFD model and experimental tests: (a) 5% uncertainty; (b) 10% uncertainty.

CO₂ measured with gas analyzer is presented in Figure 21. This plot is a set of measurements of mole fractions vs. time taken during all experimental tests. It is observed that the maximum value reached for the mole fraction of CO₂ was 0.037, the minimum value was 0.008, and the average value was 0.0127. The oscillatory behavior of measurements for mole fractions of CO₂ and CO in Figures 21 and 22 is caused by the transitory response over time of combustion during experimental tests.

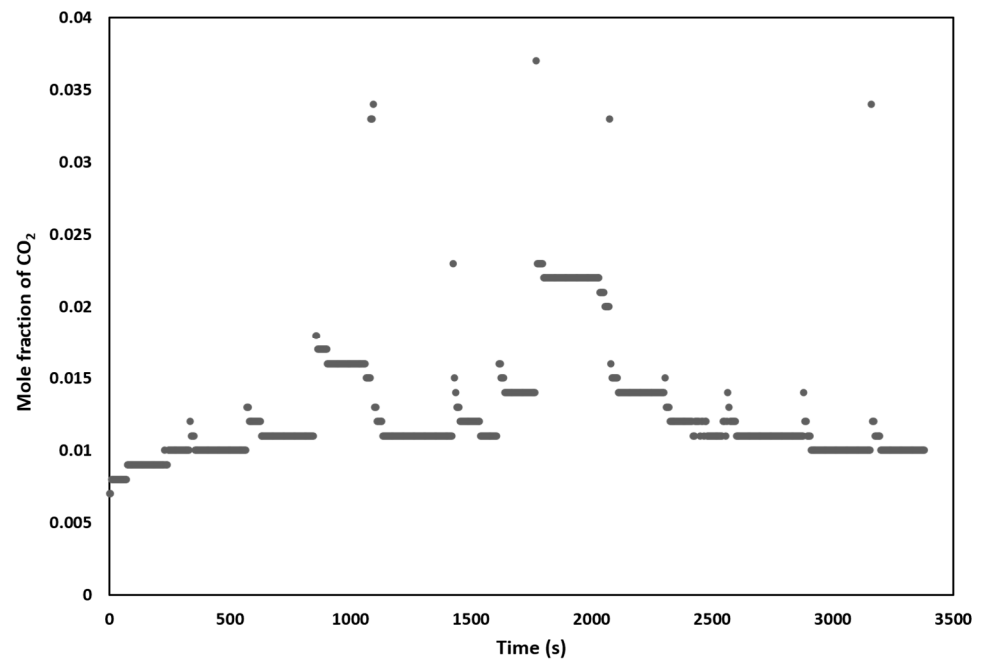


Figure 21. Results of CO₂ measurements during experimentation.

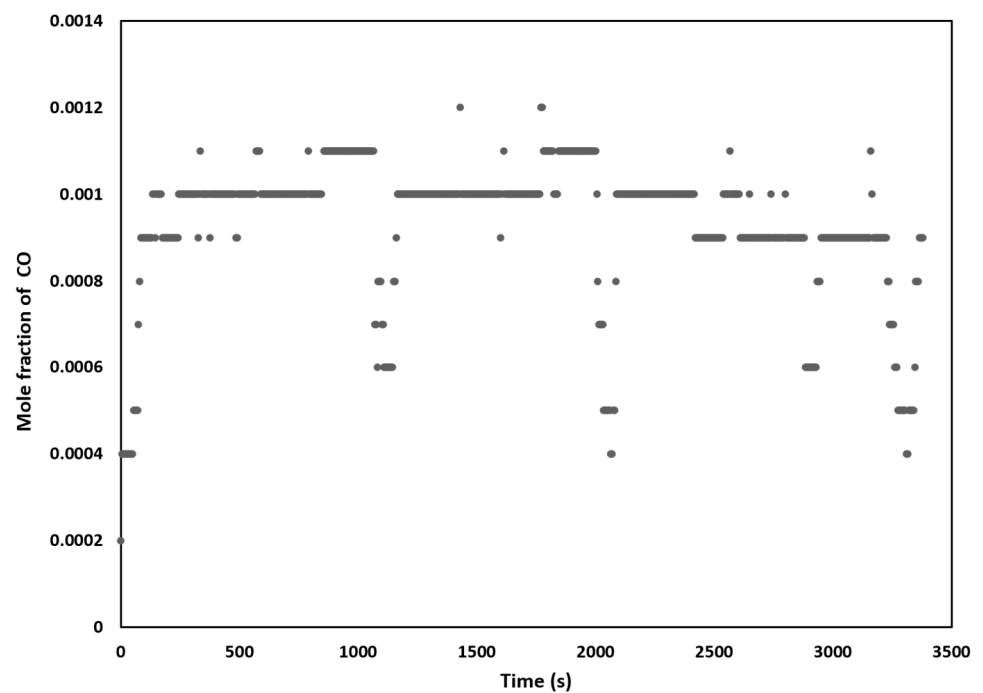


Figure 22. Results of CO measurements during experimentation.

Figure 22 shows the mole fraction of CO measured during the experiment with an average value of 0.0009, a maximum of 0.00132, and a minimum of 0.0004.

Figure 23 depicts a bar chart for the comparison of mole fractions of CO₂, CO, and NO at the nozzle outlet. The average mole fraction of CO₂ measured experimentally was 0.0127; meanwhile, its average value for the numerical model was 0.0134. It is observed that simulated data lie within 6% uncertainty of experimental data [68].

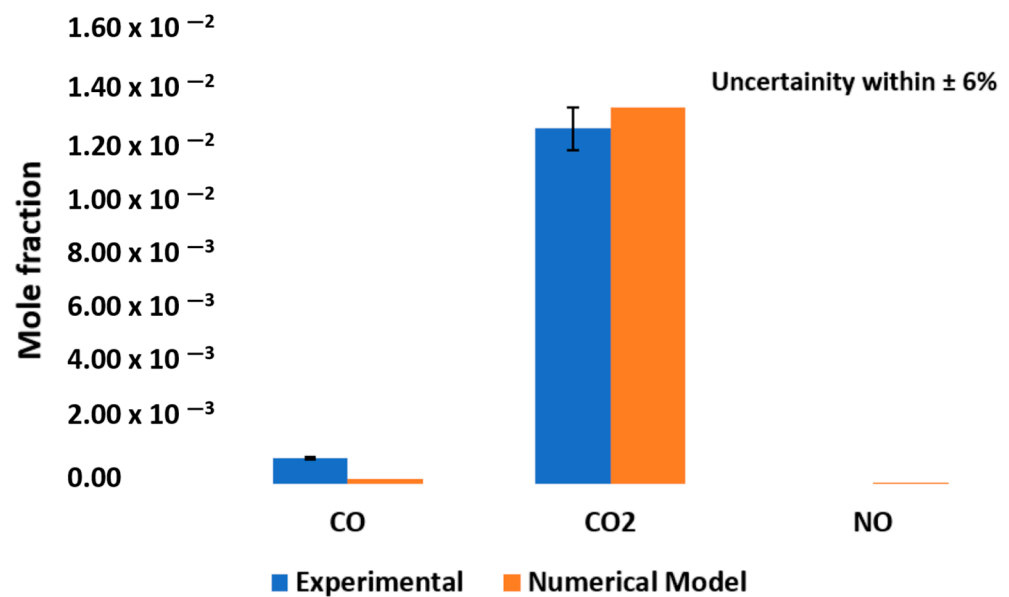


Figure 23. Comparison of numerical model and experimental data for mole fractions of CO, CO₂, and NO.

Regarding NO, data obtained by the gas analyzer for its mole fraction during experimentation indicated 0, while the numerical model resulted in an average mole fraction of 2.3×10^{-6} at the nozzle outlet. This last value could be considered as 0.

The average mole fraction of CO provided by the gas analyzer was 0.0009. On the other hand, the average value from the numerical model was 0.000145. Comparison of both values shows that numerical model value does not lie within 6% uncertainty.

6. Conclusions

The analysis of biogas combustion in a non-premixed flame CC was presented. The effect of a strong swirl on the combustion process of biogas was studied by placing a swirler (Sn of 2.48) at the airstream inlet. This analysis of combustion was performed using numerical modeling with CFD and experimental testing. Numerical analysis was performed using the $k-\epsilon$ RNG model of the renormalization group. To solve the chemical kinetics of the flame, the laminar flamelet model was used applying a medium-pass mechanism from the University of San Diego for biogas. The thermal NO_x formation mechanism was used to analyze NO emissions. Variables were measured during the experimental tests as follows: temperatures at eight points of the CC; air pressure; fuel pressure; humidity; and CO, CO₂, and NO emissions. Results obtained with the numerical modeling of biogas combustion showed the following:

- The $k-\epsilon$ RNG model in conjunction with the chemical kinetics mechanism predicted with good acceptable accuracy the behavior of the experimental testing. Temperatures measured at both peepholes of the CC have similar behavior to those obtained in the experimental testing.
- Non-premixed flame is highly influenced by a strong swirl because it generates recirculation at the center of the primary zone of the CC. Recirculation centers the flame inside the CC, and there are no hot spots near the flame tube. Biogas injection at the primary zone reduces the flame temperature in this region. The highest temperatures are located at the intermediate and dilution zones caused by a decrement in the mole fraction of CO₂ compared to the primary zone.
- A strong swirl in biogas combustion had a positive effect, given that it centers the flame in the combustion chamber and causes recirculation to promote a constant re-ignition of air–fuel mixture; this effect avoids the presence of noncombustion zones all along the biogas flame.

- Regarding emissions, experimental results indicated an average mole fraction of CO at the combustion chamber outlet of 1.45×10^{-4} . This value is below limits allowed by national legislation.
- Experimental testing resulted in a mole fraction of CO₂ at the combustion chamber outlet of 0.0127. This is far lower than the original biogas mole fraction of CO₂ of 0.25. A phenomenon inside the combustion chamber is considered to produce CO₂, which was verified with the distribution profile of CO at the dilution zone where this gas is combined with O₂ to generate CO₂. A strong swirl improved the combustion process to reduce the mole fraction of CO₂ at the combustion chamber outlet. The average mole fraction of CO₂ from the numerical model lies within 6% uncertainty with respect to experimental data.
- Formation of NO according to numerical model is observed to begin in between primary and intermediate zones. It increased gradually until reaching an average mole fraction of 2.3×10^{-6} at the outlet. The sensitivity of the gas analyzer measured a mole fraction of 0; therefore, as the mole fraction from the numerical model is close to zero, both models are similar.

This research validates that implementing a swirler with a high swirl number in biogas combustion opens the possibility for biogas to be considered as a fuel for combustion chambers with non-premixed flames. The swirler improves the burning process, thus reducing emissions of pollutants such as CO, CO₂, and NO. The swirler also avoids the existence of noncombustion zones. The numerical model developed in this research could be considered to study the behavior of flames under different mole fractions of CO₂ in the biogas mixture.

The numerical model as presented in this research could be used to accomplish goals from the Kyoto Protocol and the Paris Agreement to reduce greenhouse gas emissions.

Predicting the behavior of flames produced by the combustion of biogas combined with fuels with higher calorific value is out of the scope of this research; however, it is considered as future work to analyze the effect of hydrogen in the turbulent combustion of biogas.

Author Contributions: Conceptualization, M.O.V.-Z.; Investigation, C.A.R.-R. and M.E.T.-d.-C.; Methodology, M.O.V.-Z. and M.E.T.-d.-C.; Resources, M.E.T.-d.-C.; Software, M.E.T.-d.-C.; Supervision, M.E.T.-d.-C.; Validation, M.O.V.-Z., C.A.R.-R. and M.E.T.-d.-C.; Writing—original draft, M.E.T.-d.-C.; Writing—review & editing, A.L.H.-M. All authors have read and agreed to the published version of the manuscript.

Funding: The APC was funded by the Master in Applied Engineering of Universidad Veracruzana.

Institutional Review Board Statement: Not applicable.

Informed Consent Statement: Not applicable.

Data Availability Statement: Not applicable.

Acknowledgments: C.A.R.-R. thanks Consejo Nacional de Ciencia y Tecnología for the scholarship received during his master's studies.

Conflicts of Interest: The authors declare no conflict of interest. The funders had no role in the design of the study; in the collection, analyses, or interpretation of data; in the writing of the manuscript; or in the decision to publish the results.

References

1. Banjaa, M.; Jégardb, M.; Motola, V.; Sikkema, R. Support for biogas in the EU electricity sector—A comparative analysis. *Biomass Bioenergy* **2019**, *128*, 105313. [[CrossRef](#)]
2. Wang, J.; Xue, Q.; Guo, T.; Mei, Z.; Long, E.; Wen, Q.; Huang, W. A review on CFD simulating method for biogas fermentation material fluid. *Renew. Sustain. Energy Rev.* **2018**, *97*, 64–73. [[CrossRef](#)]
3. Kan, X.; Zhou, D.; Yang, W.; Zhai, X.; Wang, C.H. An investigation on utilization of biogas and syngas produced from biomass waste in premixed spark ignition engine. *Appl. Energy* **2018**, *212*, 210–222. [[CrossRef](#)]
4. Yilmaz, I.T.; Gumus, M. Investigation of the effect of biogas on combustion and emissions of TBC. *Fuel* **2017**, *188*, 69–78. [[CrossRef](#)]

5. Ramírez-Arpide, F.R.; Espinosa-Solares, T.; Gallegos-Vázquez, C.; Santoyo-Cortés, V.H. Bioenergy production from nopal cladodes and dairy cow manure on a farm-scale level: Challenges for its economic feasibility in Mexico. *Renew. Energy* **2019**, *142*, 383–392. [[CrossRef](#)]
6. Panesso, A.; Cadena, J.; Mora Flórez, J.J.; Ordoñez, M.C. Análisis del biogás captado en un relleno sanitario como combustible primario para la generación de energía eléctrica. *Sci. Tech.* **2011**, *XVII-47*, 23–28.
7. Liu, A.; Yang, Y.; Chen, L.; Zeng, W.; Wang, C. Experimental study of biogas combustion and emissions for a micro gas turbine. *Fuel* **2020**, *267*, 117312. [[CrossRef](#)]
8. Rosas-Mendoza, E.S.; Méndez-Contreras, J.M.; Martínez-Sibaja, A.; Vallejo-Cantu, N.A.; Lassman-Alvarado, A. Anaerobic digestion of citrus industry effluents using an Anaerobic Hybrid Reactor. *Clean Technol. Environ. Policy* **2017**, *20*, 1387–1397. [[CrossRef](#)]
9. Mosayeb Nezhad, M.; Mehr, A.S.; Lanzini, A.; Misul, D.; Santarelli, M. Technology review and thermodynamic performance study of a biogas-fed micro humid air turbine. *Renew. Energy* **2019**, *140*, 407–418. [[CrossRef](#)]
10. Ehsan Hosseini, S.; Abdul Wahid, M. Development of biogas combustion in combined heat and power generation. *Renew. Sustain. Energy Rev.* **2014**, *40*, 868–874. [[CrossRef](#)]
11. Soares, J.; Oliveira, A.C. Numerical simulation of a hybrid concentrated solar power/biomass mini power plant. *Appl. Thermal Eng.* **2017**, *111*, 1378–1386. [[CrossRef](#)]
12. Al-Rashed, A.A.A.A.; Afrand, M. Multi-criteria exergoeconomic optimization for a combined gas turbine-supercritical CO₂ plant with compressor intake cooling fueled by biogas from anaerobic digestion. *Energy* **2021**, *223*, 119997. [[CrossRef](#)]
13. Movahed, P.; Akram, A. Techno-Economic optimization of biogas-fueled micro gas turbine cogeneration systems in sewage treatment plant. *Energy Convers. Manag.* **2020**, *218*, 112965. [[CrossRef](#)]
14. Liu, F.; Guo, H.; Smallwood, G.J. The chemical effect of CO₂ replacement of N₂ in air on the burning velocity of CH₄ and H₂ premixed flames. *Combust. Flame* **2003**, *133*, 495–497. [[CrossRef](#)]
15. Lafay, Y.; Taupin, B.; Martins, G.; Cabot, G.; Renou, B.; Boukhalfa, A. Experimental study of biogas combustion using a gas turbine configuration. *Exp. Fluids* **2007**, *43*, 395–410. [[CrossRef](#)]
16. Gómez Montoya, J.P.; Olsen, D.B.; Amell, A.A. Engine operation just above and below the knocking threshold, using a blend of biogas and natural gas. *Energy* **2018**, *153*, 719–725. [[CrossRef](#)]
17. Colorado, A.; McDonell, V. Emissions and stability performance of a low-swirl burner operated on simulated biogas fuel in a boiler environment. *Appl. Therm. Eng.* **2020**, *130*, 1507–1519. [[CrossRef](#)]
18. Vera-Romero, I.; Martínez-Reyes, J.; Estrada-Jaramillo, M.; Ortiz-Soriano, A. Biogas and Power Generation Potential Part I: Bovine and Pig Manure. *Ing. Investig. Y Tecnol.* **2013**, *15*, 429–436.
19. Salzano, E.; Basco, A.; Cammarota, F.; Di Sarli, V.; Di Benedetto, A. Explosions of Syngas/CO₂ mixtures in oxygen-enriched air. *Ind. Eng. Chem. Res.* **2012**, *51*, 7671–7678. [[CrossRef](#)]
20. Di Benedetto, A.; Di Sarli, A.; Salzano, E.; Cammarota, F.; Russo, G. Explosion behavior of CH₄/O₂/N₂/CO₂ and H₂/O₂/N₂/CO₂ mixtures. *Int. J. Hydrog. Energy* **2009**, *34*, 6970–6978. [[CrossRef](#)]
21. Bulat, G.; Liu, K.; Brickwood, G.; Sanderson, V. Intelligent operation of Siemens (SGT-300) DLE gas turbine combustion system over an extended fuel range with low emissions. In Proceedings of the ASME 2011 Turbo Expo: Turbine Technical Conference and Exposition, Vancouver, BC, Canada, 6–10 June 2011; Volume 2, pp. 917–925.
22. Asti, A.; Stewart, J.; Forte, A.; Yilmaz, E.; D’Ercole, M. Enlarging the Fuel Flexibility Boundaries: Theoretical and Experimental Application to a New Heavy-Duty Gas Turbine (MS5002E). In Proceedings of the ASME Turbo Expo 2008: Power Land Sea Air, Berlin, Germany, 9–13 June 2008; Volume 3, pp. 553–563.
23. Peters, N. Fifteen Lectures on Laminar and Turbulent Combustion. *Ercoftac Summer Sch.* **1992**, *1428*, 245.
24. Bilger, R.W.; Pope, S.B.; Bray, K.C.; Driscoll, J.F. Paradigms in turbulent combustion research. *Proc. Combust. Inst.* **2005**, *30*, 21–42. [[CrossRef](#)]
25. Veynante, D.; Vervisch, L. Turbulent combustion modeling. *Prog. Energy Combust. Sci.* **2002**, *28*, 193–266. [[CrossRef](#)]
26. Tangirala, V.; Driscoll, J.F. Temperatures within Non-premixed Flames: Effects of Rapid Mixing Due to Swirl. *Combust. Sci. Technol.* **1988**, *60*, 143–162. [[CrossRef](#)]
27. Roubík, H.; Mazancová, J. Suitability of small-scale biogas systems based on livestock manure for the rural areas of Sumatra. *Environ. Dev.* **2020**, *33*, 100505. [[CrossRef](#)]
28. Dalpaz, R.; Konrad, O.; Silva Cyrne, C.C.; Panis Barzotto, H.; Hasan, C.; Guerini Filho, M. Using biogas for energy cogeneration: An analysis of electric and thermal energy generation from agro-industrial waste. *Sustain. Energy Technol. Assess.* **2020**, *40*, 100774. [[CrossRef](#)]
29. Zavaleta Luna, D.A.; Viguera Zúñiga, M.O.; Herrera May, A.L.; Zamora Castro, S.A.; Tejeda del Cueto, M.E. Optimized design of a Swirler for a combustion chamber of non-premixed flame using genetic algorithms. *Energies* **2020**, *13*, 2240. [[CrossRef](#)]
30. Khodabandeh, E.; Moghadasi, H.; Pour, M.S.; Ersson, M.; Jönsson, P.G.; Rosen, M.A.; Rahbari, A. CFD study of non-premixed swirling burners: Effect of turbulence models. *Chin. J. Chem. Eng.* **2020**, *28*, 1029–1038. [[CrossRef](#)]
31. Beer, M.; Syred, N. Combustion in Swirling Flows: A Review. *Combust. Flame* **1974**, *23*, 143–201.
32. Yuasa, S. Effects of swirl on the stability of jet diffusion flames. *Combust. Flame* **1986**, *66*, 181–192. [[CrossRef](#)]
33. Coghe, A.; Solero, G.; Schribano, G. Recirculation phenomena in a natural gas swirl combustor. *Experimental Thermal and Fluid. Science* **2004**, *28*, 709–714.

34. Jerzak, W.; Kuznia, M. Experimental study of impact of swirl number as well as oxygen and carbon dioxide content in natural gas combustion air on flame flashback and blow-off. *J. Nat. Gas Sci. Eng.* **2016**, *29*, 46–54. [CrossRef]
35. Mordaunt, C.J.; Pierce, W.C. Design and preliminary results of an atmospheric-pressure model gas turbine combustor utilizing varying CO₂ doping concentration in CH₄ to emulate biogas combustion. *Fuel* **2014**, *124*, 258–268. [CrossRef]
36. Tejada del Cueto, M.E.; Viguera Zúñiga, M.O.; Welsh Rodríguez, C.M.; Marín Urías, L.F.; Herrera May, A.L.; Ordoñez Romer, C.L. Alineamiento de flama usando placas perforadas Tándem en una cámara de combustión de gas LP. *Rev. La Soc. Mex. Ing. Mecánica* **2015**, *5*, 293–302.
37. Slefarski, R.; Sacha, J.; Grzymislawski, P. Combustion of mixtures of biogas and syngases with methane in strong swirl flow. In Proceedings of the 6th European Combustion Meeting, Lund, Sweden, 25–28 June 2013; pp. 117–128.
38. Zhao, Y.; McDonell, V.; Samuelsen, S. Assessment of the combustion performance of a room furnace operating on pipeline natural gas mixed with simulated biogas or hydrogen. *Int. J. Hydrog. Energy* **2020**, *45*, 11368–11379. [CrossRef]
39. Dai, W.; Qin, C.; Chen, Z.; Tong, C.; Liu, P. Experimental studies of flame stability limits of biogas flame. *Energy Convers. Manag.* **2012**, *63*, 157–161. [CrossRef]
40. Benato, A.; Macor, A.; Rossetti, A. Biogas engine emissions: Standards and on-site measurements. *Energy Procedia* **2017**, *126*, 398–405. [CrossRef]
41. Sahin, M.; Ilbas, M. Analysis of the effect of H₂O content on combustion behaviours of a biogas fuel. *Int. J. Hydrog. Energy* **2020**, *45*, 3651–3659. [CrossRef]
42. Fischer, M.; Jiang, X. Numerical studies of CO formation during biogas combustion. *Energy Procedia* **2017**, *142*, 426–431. [CrossRef]
43. Wu, B. Advances in the use of CFD to characterize, design and optimize bioenergy systems. *Comput. Electron. Agric.* **2013**, *93*, 195–208. [CrossRef]
44. Granell Ruiz, R. *Análisis del Flujo Ambiental y Propuesta Metodológica Para Simulaciones CFD Aplicadas a la Ventilación Natural de Invernaderos*; Universidad Politécnica de Valencia: Valencia, Spain, 2014.
45. Givi, P. Model-free simulations of turbulent reactive flows. *Prog. Energy Combust. Sci.* **1989**, *15*, 1–107. [CrossRef]
46. Huang, Y.; Yang, V. Dynamics and stability of lean-premixed swirl-stabilized combustion. *Prog. Energy Combust. Sci.* **2009**, *35*, 293–364. [CrossRef]
47. Yan, Y.W.; Zhao, J.X.; Zhang, J.Z.; Liu, Y. Large-eddy simulation of two-phase spray combustion for gas turbine combustors. *Appl. Therm. Eng.* **2008**, *28*, 1365–1374.
48. Bulat, G.; Jones, W.P.; Marquis, A.J. Large eddy simulation of an industrial gas-turbine combustion chamber using the sub-grid PDF method. *Proc. Combust. Institut.* **2013**, *34*, 3155–3164. [CrossRef]
49. Giacomazzi, E.; Battaglia, V.; Bruno, C. The coupling of turbulence and chemistry in a premixed bluff-body flame as studied by LES. *Combust. Flame* **2004**, *138*, 320–335. [CrossRef]
50. Jenny, P.; Roekaerts, D.; Beishuizen, N. Modeling of turbulence dilute spray combustion. *Prog. Energy Combust. Sci.* **2012**, *38*, 846–887. [CrossRef]
51. Vondál, J.; Hájek, J. Prediction of flow through swirl generator and validation by measured data. In Proceedings of the 13th European Turbulence Conference, Warsaw, Poland, 12–15 September 2011.
52. Widmann, J.F.; Charagundla, S.; Presser, C. Aerodynamic study of a vane-cascade swirl generator. *Chem. Eng. Sci.* **2000**, *55*, 5311–5320. [CrossRef]
53. Darmawan, S.; Budiarto, B.; Siswantara, A.I. CFD Investigation of standard k- and RNG k-e turbulence model in compressor discharge of proto x-2 bioenergy micro gas turbine. In Proceedings of the 8th International Conference on Fluid and Thermal Energy Conversion, Semarang, Indonesia, 8–11 November 2013; pp. 8–11.
54. Khaldi, N.; Mhiri, H.; Bournot, P. A comparative study of turbulence models performance for a 300 MWe tangentially fired pulverized-coal furnace. In Proceedings of the Fifth International Renewable Energy Congress IREC, Hammamet, Tunisia, 25–27 March 2014.
55. Zabed, H.M.; Akter, S.; Yun, J.; Zhang, Y.; Qi, X. Biogas from microalgae: Technologies, challenges, and opportunities. *Renew. Sustain. Energy Rev.* **2020**, *117*, 109503. [CrossRef]
56. Ansys. (02 de 05 de 2021). ANSYS FLUENT 12.0/12.1 Documentation–4.4.2 RNG k-e Model. Available online: <https://www.afs.enea.it/project/neptunius/docs/fluent/html/th/node59.htm> (accessed on 5 May 2021).
57. Carrillo Sánchez, J.M.; Castillo Elsitsié, L.G. Consideraciones del mallado aplicadas al cálculo de flujos bifásicos con las técnicas de dinámica de fluidos computacional. *IV Jorn. Introd. Investig. UPCT* **2011**, *4*, 33–35.
58. Yakhot, V.; Orszag, S.A. Renormalization group analysis of turbulence. I. Basic theory. *J. Sci. Comput.* **1986**, *1*, 3–51. [CrossRef]
59. Leonidivna Naidiuk, O.; Torres Jara, P. *Introducción al Análisis Térmico y de Fluidos Mediante Ansys*; Universidad Politécnica Salesiana: Quito, Ecuador, 2018.
60. Subiabre Sánchez, P.J. *Diseño básico de una Cámara de Combustión Para una Microturbina a Gas*; Universidad de Chile: Santiago, Chile, 2017.
61. Peters, N. Diffusion flamelet models in non-premixed turbulent combustion. *Prog. Energy Combust. Sci.* **1984**, *10*, 319–339. [CrossRef]
62. Jahangirian, S.; Engeda, A. Biogas combustion and chemical kinetics for gas turbine applications. In Proceedings of the ASME 2008 International Mechanical Engineering Congress and Exposition, Boston, MA, USA, 31 October–6 November 2008; Volume 3, p. 48647.

63. Peters, N. Multiscale combustion and turbulence. *Proc. Combust. Inst.* **2009**, *32*, 1–25. [[CrossRef](#)]
64. Alfaro Anaya, J.A.; Gallegos Muñoz, A.; Riesco-Ávila, J.M.; Flores López, M.; Campos Amezcua, A.; Mani-González, A.G. Analysis of the flow in the combustor-transition piece considering the variation in the fuel combustion. *J. Therm. Sci. Eng. Appl.* **2011**, *3*, 021003. [[CrossRef](#)]
65. Combustion Research Group at UC San Diego. Available online: <http://web.eng.ucsd.edu/mae/groups/combustion/index.html> (accessed on 26 February 2021).
66. Valera Medina, A.; Synred, N.; Abdulsada, M. Flashback analysis in tangential swirl burners. *Ing. Investig. Y Tecnol.* **2010**, *12*, 487–497.
67. Saediamiri, M.; Birouk, M.; Kozinski, J.A. On the stability of a turbulent non-premixed biogas flame: Effect of low swirl strength. *Combust. Flame* **2014**, *161*, 1326–1336. [[CrossRef](#)]
68. Maupin, K.A.; Swiler, L.P.; Porter, N.W. Validation metrics for deterministic and probabilistic data. *J. Verif. Valid. Uncert.* **2018**, *3*, 031002. [[CrossRef](#)]